energies

MDPI

Article

CFD Analysis on the Heat Transfer and Fluid Flow of Solar Air Heater having Transverse Triangular Block at the Bottom of Air Duct

Hwi-Ung Choi and Kwang-Hwan Choi *

Department of Refrigeration and Air-Conditioning Engineering, Pukyong National University, Busan 48513, Korea; nopoil@naver.com

* Correspondence: choikh@pknu.ac.kr; Tel.: +81-51-629-6179; Fax: +82-51-629-6174

Received: 10 February 2020; Accepted: 25 February 2020; Published: 2 March 2020

Abstract: In this study, a two-dimensional CFD (computational fluid dynamics) analysis was performed to investigate the heat-transfer and fluid-friction characteristics in a solar air heater having a transverse triangular block at the bottom of the air duct. The Reynolds number, block height (e), pitch (P), and length (l) were chosen as design parameters. The results are validated by comparing the Nusselt number predicted by simulation with available experimental results. Renormalization-group (RNG) k-ε model with enhanced wall-treatment was selected as the most appropriate turbulence model. From the results, it was found that the presence of a transverse triangular block produces a higher Nusselt number than that of smooth air duct. The enhancement in Nusselt number varied from 1.19 to 3.37, according to the geometric conditions investigated. However, the use of transverse triangular block also results in significantly higher friction losses. The thermohydraulic performance (THPP) was also estimated and has a maximum value of 1.001 for height (e) of 20 mm, length (l) of 120 mm, and pitch (P) of 150 mm, at Reynolds number of 8000. Furthermore, in the present study, correlations of the Nusselt number and friction factor were developed as a function of geometrical conditions of the transverse triangular block and Reynolds number, which can be used to predict the value of Nusselt number and friction factor with the absolute percentage deviations of 3.29% and 7.92%, respectively.

Keywords: solar air heater; solar collector; Nusselt number; CFD; friction factor

1. Introduction

The solar air heater is one of the basic and widely used pieces of equipment that can convert solar energy into useful thermal energy. The solar air heaters are cheap due to the simple design, and they are widely used in domestic and industrial applications. The main applications of solar air heaters are space heating, drying the crops and fruit, curing of products, and so on. A solar air heater has a simple design and is economic because of the little maintenance. However, the heat-transfer performance between flowing air and the absorber plate is low due to the low thermal conductivity of air, and it leads to low thermal efficiency.

One of the most widely used methods to increase the heat transfer coefficient is mounting artificial roughness on the absorber plate. The artificially roughened absorber plate can create turbulence near to a heated absorber that can break the viscous sublayer and allow the mixing of faster flowing air in the outer region with low velocity air near the wall, leading to the higher heat transfer [1,2]. Yadav and Bhagoria [3–5] conducted a CFD analysis on the heat-transfer performance and fluid-friction characteristics in a solar air heater artificially roughened with a repeated transverse circular, triangular, and rectangular rib. Singh et al. [6] examined the heat-transfer and fluid-friction characteristics of

solar air heater having non-uniform cross-section transverse rib roughness on the absorber plate. Akpinal and Koçyiğit [7] analyzed the performance of a solar air heater supplied with various obstacles experimentally. Singh et al. [8] evaluated the effect of multiple arc-shaped ribs on the heat-transfer and friction characteristics, with various geometrical parameters. Singh et al. [9] investigated the heat and fluid-flow characteristics in a rectangular duct roughened with periodic discrete V-down rip. Kumar and Kim conducted a CFD-based analysis to investigate heat transfer and friction characteristics in rectangular channel with discrete multi-V-pattern ribs [10].

The other method to improve the performance of a solar air heater is modifying the absorber plate. Karim and Hawlader [11] examined the performance of three types of solar air collectors having a flat-plate, v-corrugated, and finned absorber. Ho et al. [12] conducted an experimental and theoretical analysis of the double-pass cross-corrugated and double-pass V-corrugated solar air collector. Zheng et al. [13] performed experimental investigation of solar air heaters having perforating corrugated plate, slit-perforated plate, and corrugated packing. In addition to this, a number of studies have been conducted, and they mainly focused on the performance improvement by artificially roughened rip mounted on the absorber plater or modified absorber structure [14–17].

Another technique to increase the heat-transfer performance of solar air heater is modifying the air duct or the shape of bottom plate in an air channel of the solar air heater. Ho et al. [18] analyzed the performance of double-pass cross-corrugated solar air collector that has the wavelike-shaped absorbing plate and bottom plate. Singh [19] investigated the thermal performance of solar air heaters that have semicircular and triangular cross-sectioned duct under external recycle. This model is relatively simple to make and easier to install than the other methods. Moreover, this method can be combined with a solar air heater with an artificially roughened absorber.

However, it is observed that very few studies on heat-transfer enhancement by modification of air duct or bottom plate have been done different with the studies that investigated the effect of artificially roughened rib or modified structure of absorber plate. Thus, in this study, the thermal performance of a solar air heater with a transverse triangular block at the bottom plate was investigated by CFD analysis. It is one of the modifications of the bottom plate, and the block shape was employed as a triangle, which is one simple shapes. The main purposes of the present study were as follows: (a) to investigate the effect of geometric conditions of transverse triangular block on the heat-transfer improvement and pressure-drop increase; (b) to develop the correlations of Nusselt number and friction factor that can use to predict; and (c) to confirm the feasibility of the new designed air duct having a transverse triangular block.

2. Methodology

2.1. Description of Computational Model

Figure 1a,b shows a schematic of the solar air heater, which has a transverse triangular block. The simulation model is a single-flow, single-pass solar air heater and the transverse triangular block installed at the bottom plate of an air duct. The two-dimensional solution domain was used for CFD analysis in order to simplify the analysis. Figure 2 shows a schematic of the computational domain. The flow cross-section of the duct is 80 mm × 500 mm. The length of the test section was 1800 mm. The hydraulic diameter (D_h) and aspect ratio (W/H) were 0.138 and 6.25, respectively. Moreover, the entrance duct and exit duct were installed at the test section, in order to establish thermally fully developed flow and decrease the end effect in the test section [20]. The entrance duct and exit duct length was 400 and 700 mm, respectively. In the present work, twenty-seven different configurations of a transverse triangular block were simulated. Each configuration was investigated on four different Reynolds number ranges from 8000 to 20,000 generally used in a solar air heater [21–23]. Thus, 108 sets of CFD simulations having different combinations of height (e), pitch (P), length (l), and Reynolds numbers were conducted. Table 1 shows geometric parameters for solar air heater with a transverse triangular block.

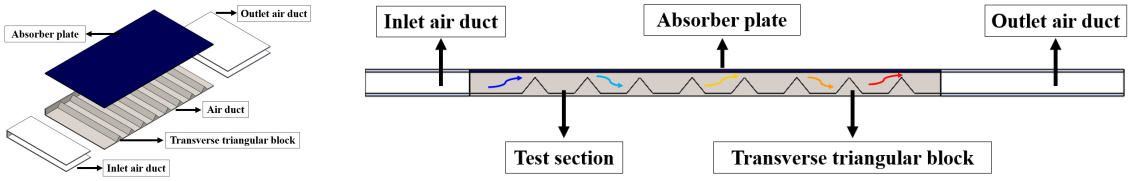

(**a**) Exploded view (**b**) Side view

Figure 1. Schematics of the solar air heater with a transverse triangular block at the bottom of air duct.

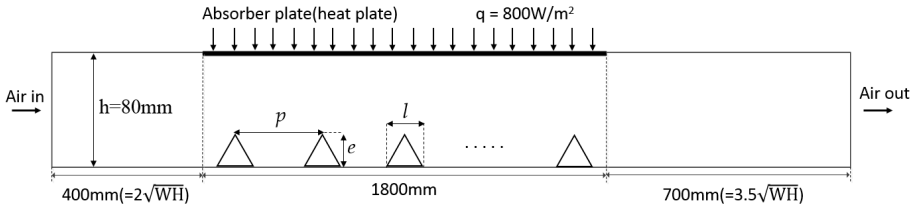

Figure 2. Schematics of the two-dimensional computational domain.

Table 1. Geometric parameters for solar air heater with a transverse triangular block at the bottom of air duct.

Parameters		Value	Parameters	Value	Parameters	Value
Duct length (mm)	Entrance	400	Duct height (mm)	80	e (mm)	20, 40, 60
	Test section	1800	Duct width (mm)	500	P (mm)	120, 150, 180
	Exit	700	Hydraulic diameter, D_h(-)	0.138	l (mm)	10, 65, 120

2.2. CFD Setup and Boundary Conditions

The investigation was performed by using ANSYS Fluent 17.1. To prepare the 2D fluid domain for numerical analysis, ANSYS Design Modeler was used. T grid was generated by using ANSYS ICEM CFD, and then the meshed model was exported to ANSYS FLUENT. The simulation model was steady incompressible turbulence flow. The pressure-based type and absolute velocity formulation were chosen as a solver in the general setup. In order to include the heat transfer and turbulence flow, the energy model and the renormalization-group (RNG) k-ε model with enhanced wall treatment in viscosity were used in the models. The solver was a segregated solution algorithm with a finite volume-based technique. A second-order upwind scheme was employed for continuity, momentum, and energy equations in the solution. The SIMPLE algorithm, which was developed by Patankar [24], was used for discretization of governing equations [25]. The convergence limit of 10^{-3} for relative deviation of continuity, 10^{-3} for relative deviation of velocity components, and 10^{-6} for relative deviation of energy was taken. To simulate solar radiation introduced on the absorber plate, both ANSYS solar calculator and uniform heat flux can be used. In the solar calculator, the value of solar radiation depends on global position, orientation, day of year, and time of day can be obtained [26,27]. However, our study focused on the effect of transvers triangular block installed at the bottom of air duct on the heat-transfer performance and fluid-flow characteristics. In many related previous studies, the uniform heat flux was applied as a boundary condition to investigate the heat-transfer performance and fluid-flow characteristics of solar air heaters [2–6,8–10,19,25,28–30]. Thus, in this work, the uniform heat flux was chosen as a boundary condition to simulate solar energy.

A constant heat flux of 800 W/m^2 was applied on the top surface of the solar air heater, while the adiabatic was applied for other walls. A uniform air velocity was applied at the air inlet. The average inlet velocity was obtained from the Reynolds number. A fixed pressure of 101,325 Pa was applied at the air outlet. The air temperature inside the air duct was taken as 300 K, at the beginning. All of the

solid surface was assumed as no-slip conditions. The turbulence intensity at the inlet can be obtained from Equation (1), as reported in Reference [31].

$$I = 0.16Re^{-1/8} \tag{1}$$

The range of operating parameters used in this computational analysis are summarized in Table 2.

Table 2. Range of operating parameters for computational investigation.

Parameters	Range	Parameters	Range
Uniform heat flux, 'q' (W/m^2)	800	*e*/*h* (-)	0.25–0.75 (3 values)
Reynolds number (-)	8000, 12,000, 16,000, 20,000	*p*/*e* (-)	2–9 (8 values)
Prandtl number of air (-)	0.7442	*l*/*e* (-)	0.16667–6 (9 values)

2.3. Governing Equations

The steady incompressible turbulence flow in a solar air heater with a transverse triangular block at the bottom of its air duct is governed by the continuity, momentum, and energy equations. With assumptions of steady state, incompressible fluid, and turbulence flow, the governing equations for two-dimensional CFD analysis can be described as follows [31].

Continuity equation:

$$\frac{\partial}{\partial x_i}(\rho u_i) = 0 \tag{2}$$

Momentum equation:

$$\frac{\partial}{\partial x_j}\left(\rho u_i u_j\right) = \frac{\partial p}{\partial x_i} + \frac{\partial p}{\partial x_j}\left[\mu\left(\frac{\partial u_i}{\partial x_j} + \frac{\partial u_j}{\partial x_i}\right)\right] + \frac{\partial}{\partial x_j}\left(-\rho\overline{u_i' u_j'}\right) \tag{3}$$

Energy equation:

$$\frac{\partial}{\partial x_i}(\rho u_i T) = \frac{\partial}{\partial x_j}\left[\left(\frac{\mu}{Pr} + \frac{\mu_t}{Pr_t}\right)\frac{\partial T}{\partial x_j}\right] \tag{4}$$

Equations (2) and (3) are also called Reynolds-averaged Navier-Stokes equations. Additional terms $-\rho\overline{u_i' u_j'}$ in Equation (3) are known Reynolds stresses, which represent the turbulence effect. In order to close Equation (3), these terms must be modeled. The Boussinesq hypothesis is a common method to relate the Reynolds stresses to the mean velocity gradients:

$$-\rho\overline{u_i' u_j'} = \mu_t\left(\frac{\partial u_i}{\partial x_j} + \frac{\partial u_j}{\partial x_i}\right) \tag{5}$$

The Boussinesq hypothesis is used not only in the k-ε models but also in the k-ω models, and this approach has a lower computational cost.

In this study, the RNG k-ε model was used with enhanced wall treatment. In the RNG k-ε model, both turbulence kinematic energy (k) and turbulence rate dissipation (ε) can be obtained from the following transport equations [31]:

$$\frac{\partial}{\partial x_i}(\rho k u_i) = \frac{\partial}{\partial x_j}\left(\alpha_k \mu_{eff}\frac{\partial k}{\partial x_j}\right) + G_k - \rho\varepsilon \tag{6}$$

$$\frac{\partial}{\partial x_i}(\rho \varepsilon u_i) = \frac{\partial}{\partial x_j}\left(\alpha_\varepsilon \mu_{eff}\frac{\partial \varepsilon}{\partial x_j}\right) + C_{1\varepsilon}\frac{\varepsilon}{k}(G_k) - C_{2\varepsilon}\rho\frac{\varepsilon^2}{k} - R_\varepsilon \tag{7}$$

In these equations, G_k is turbulence kinetic energy generation, which is caused by the mean velocity gradients. The α_k and α_ε represent the inverse effective Prandtl numbers for k and ε, respectively. μ_{eff} represents the effective turbulence viscosity and is defined as follows:

$$\mu_{eff} = \mu + \mu_t \tag{8}$$

The turbulence viscosity, μ_t, is computed by combining k and ε, as follows:

$$\mu_t = \rho C_\mu \frac{k^2}{\varepsilon} \tag{9}$$

The model constants $C_{1\varepsilon}$, $C_{2\varepsilon}$, C_μ, α_k, and α_ε are 1.42, 1.68, 0.0845, 1.39, and 1.39, respectively.

2.4. Selection of Turbulence Model and Validation

The selection of turbulence model and validation was carried out by comparing Nusselt number predicted by various turbulence models in smooth air duct with Nusselt number calculated by the Dittus-Boelter empirical correlation in Equation (10):

$$Nu_s = 0.023 Re^{0.8} Pr^{0.4} \tag{10}$$

Four turbulence models, namely a standard k-ε model with enhanced wall treatment, RNG k-ε model with enhanced wall treatment, realizable k-ε model with enhanced wall treatment, and shear stress transport (SST) k-ω model, were tested for smooth air duct.

Figure 3 shows the Nusselt number values with Reynolds number for smooth air duct, using different turbulence models. The Nusselt number values calculated by Equation (10) is plotted in the figure, for comparison. As a result, the Nusselt number values predicted by the RNG k-ε model with enhanced wall treatment resulted in an absolute percentage deviation of 2.64% from the Nusselt number values calculated by Dittus-Boelter empirical correlations. The deviation, which was obtained by 2D analysis, is similar or less than those in previous studies using 3D CFD analysis for solar air heaters [28–30]. Thus, the results of the two-dimensional CFD approximation can be regarded as a reasonable value. Predictions by the other turbulence models have shown more absolute percentage deviation with the results of empirical correlation. Thus, in the present paper, the RNG k-ε model with enhanced wall treatment was chosen for analysis.

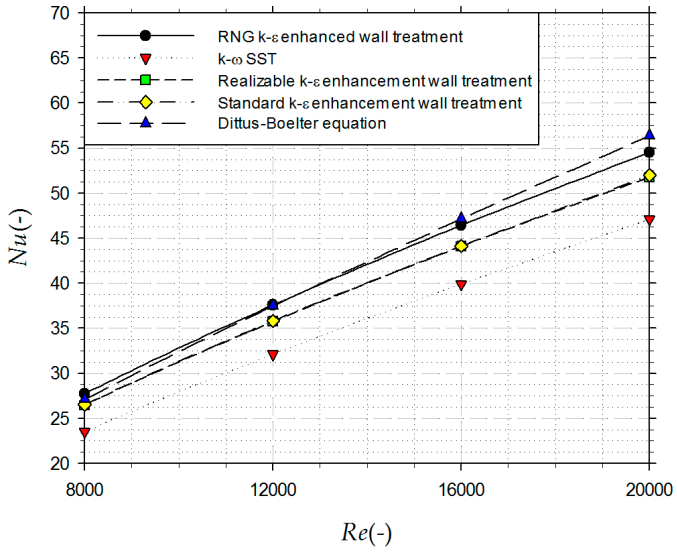

Figure 3. Comparison of Nusselt number predicted by different turbulence models with Dittus-Boelter empirical correlation for smooth duct.

2.5. Data Reduction and Grid Independence

The interest parameters for this study are the increase in heat-transfer coefficient and pressure drop by the transverse triangular block installed at the bottom of the air duct. These parameters can be represented as the Nusselt number and friction factor. The average Nusselt number that represents heat-transfer performance from the absorber to the flowing air is defined as follows:

$$Nu = hD_h/k \tag{11}$$

where h, D_h, and k are the convective heat-transfer coefficient, the hydraulic diameter of the air duct, and the thermal conductivity of air, respectively.

Friction factor that represents pressure drop can be obtained by the following calculation:

$$f = \frac{(\Delta P/L)D_h}{2\rho v^2} \tag{12}$$

where, ΔP, ρ, and v are pressure drop across the test section, air density, and average velocity of air.

The presence of the transverse triangular block installed at the bottom of the air duct results in a heat-transfer enhancement. However, this enhancement accompanies a remarkable increase in the friction factor. Thus, the thermohydraulic performance parameter (THPP) was suggested by Webb and Eckert [32], as it evaluates the overall performance of the solar air heater, including both heat-transfer enhancement and increase in the friction factor. This parameter has been widely used to evaluate the performance of solar air heaters in the previous studies [3–5,10,28–30] and is defined as follows:

$$\text{THPP} = \frac{(Nu_b/Nu_s)}{(f_b/f_s)^{1/3}} \tag{13}$$

It has also been known as thermoaerodynamic [26] and thermal enhancement factor [33,34]

Before detailed investigation, a grid independence test was performed for a solar air heater that has a transverse triangular block. First, the initial mesh was generated with 1 mm of cell size. Subsequently, the mesh became finer with each gradient adaptation for temperature, velocity, pressure, wall shear stress, and turbulence intensity, which made fine mesh in the areas where the gradient values was more than 1% of the maximum values in each parameter, as shown in Figure 4a–f. The number of cells and Nusselt number after each gradient adaptation for a fixed value of height (e), pitch (P), and length (l), at a Reynolds number value of 12,000, are tabulated in Table 3.

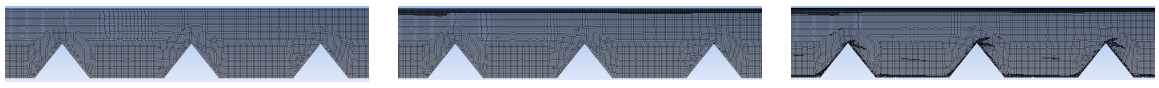

(**a**) No adaptation

(**b**) Temperature gradient adaptation

(**c**) Velocity gradient adaptation

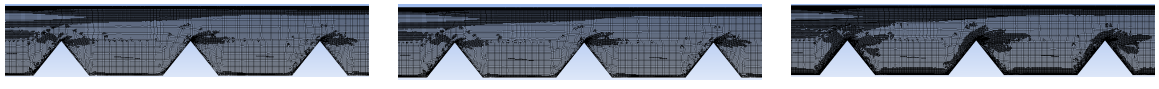

(**d**) Pressure gradient adaptation

(**e**) Wall shear stress gradient adaptation

(**f**) Turbulence intensity gradient adaptation

Figure 4. Grid system after successive gradient adaptations for a fixed value of pitch (P = 150 mm) and length (l = 65 mm), and different value of height (e) at Reynolds number of 12,000.

Table 3. Number of cells and Nusselt number after each gradient adaptation for a solar air heater with a transverse triangular block at the bottom of the air duct for fixed value of height (e = 40 mm), pitch (P = 150 mm), length (l = 65 mm), and Reynolds number (Re = 12,000).

Gradient Adaptation	Number of Cell	Nusselt Number	Percent Change in Number of Cell (%)	Percent Change in Nusselt Number (%)
No adaptation	211,920	83.117	-	-
I Adaptation—temperature	239,385	80.306	12.960	3.382
II Adaptation—velocity	320,886	79.898	34.046	0.508
III Adaptation—pressure	489,672	77.730	52.600	2.713
IV Adaptation—wall shear stress	496,149	77.706	1.323	0.031
V Adaptation—turbulence intensity	647,814	77.647	30.568	0.076

From the table, it can be seen that the percent of variation of the Nusselt number is negligible, even though the mesh is made finer. Therefore, the results can be regarded as a grid independent. Thus, in all investigation, the gradient adaptations were conducted to make all of the results to grid independent.

3. Results and Discussion

The effects of various flow and geometric conditions of a transverse triangular block on the heat-transfer performance and friction characteristics in an air duct of solar air heater are presented below.

3.1. Heat Transfer

In this section, the heat-transfer increase in the solar air heater with a transverse triangular block at the bottom of air duct is presented as an average Nusselt number.

Figure 5a–c shows the variation of average Nusselt number for different values of pitch (P), length (l), and height (e) for transverse triangular block as a function of Reynolds number. In all cases, the presence of the transverse triangular block leads to a superior average Nusselt number, as expected. The transverse triangular block can result in higher heat-transfer performance than that of a smooth air duct because of the increase in local velocity induced by the block. From the results, it is seen that the average Nusselt number increases as the Reynolds number increases. The velocity increases as the Reynolds number increases, resulting in an improved heat-transfer rate.

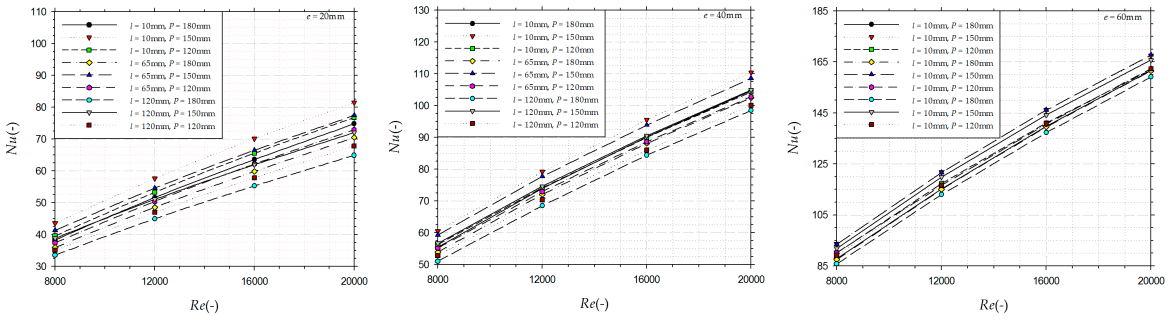

(**a**) e = 20 mm (**b**) e = 40 mm (**c**) e = 60 mm

Figure 5. Nusselt number for different value of pitch (P), length (l), and for a fixed value of height (e) with Reynolds number.

The average Nusselt number increases as the height (e) increases for a fixed value of pitch (P), length (l), and Reynolds number. This is due to the higher increase in local velocity, as can be seen velocity contour in Figure 6a–c. The maximum air velocity near the heat plate increases as the height (e) increases for a fixed value of Reynolds number, which causes an increase in heat transfer performance.

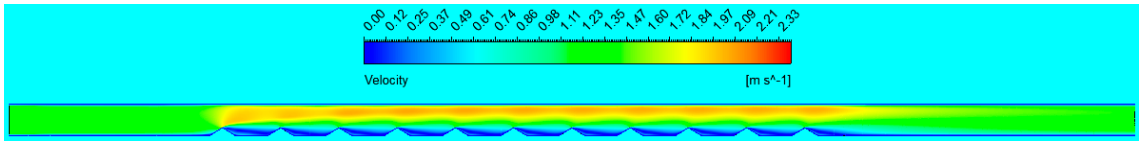

(**a**) e = 20 mm

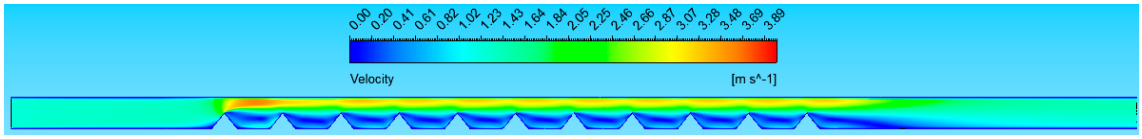

(**b**) e = 40 mm

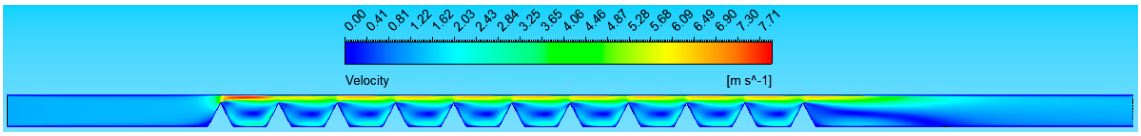

(**c**) e = 60 mm

Figure 6. Velocity contours at Reynolds number of 12,000 for a fixed value of pitch (P = 150 mm) and length (l = 65 mm), and different value of height (e).

From the results, it can be also seen that the average Nusselt number increases and then decreases as the pitch (P) increases for a fixed value of height (e), length (l), and Reynolds number. The number of blocks increases as the pitch (P) decreases. As the number of blocks increase, the flow acceleration region increases, resulting in a higher average Nusselt number. However, the average Nusselt number decreases when the pitch (P) is as small as 120 mm. This may be due to the decrease in mixing of upper and lower air, since the air mainly flows to the top side as the number of blocks increases. The decrease in mixing of upper and lower flowing air leads to the decrease in temperature difference between heat plate and air, which results in lower heat-transfer performance.

Figure 7a–c shows the temperature of heat plate and air in a test section with x–position at a fixed value of Reynolds number (Re = 12,000) for a fixed value of height (e = 40 mm), length (l = 65 mm), and for different values of pitch (P). The air temperature for the pitch (P) of 150 mm was found to be less than the other pitches (P). It indicates higher mixing of flowing air causing a decrease in temperature of the heat plate, resulting in the increase in heat-transfer coefficient. From the figure, the temperature of the heat plate for a pitch (P) of 150 mm was found to be less than the other pitches (P), as expected. In addition to this, the average Nusselt number decreases as the length (l) increases for a fixed value of height (e), pitch (P), and Reynolds number. This is due to the increase in surface friction, which causes the decrease in local velocity. Figure 8a–c shows velocity contour for different values of length (l) for a fixed height (e = 40 mm), pitch (p = 150 mm), and Reynolds number (Re = 12,000). The scale of velocity remains same, but the contour structure changes with the change in length (l). From the figure, it is observed that the maximum velocity decreases with the increase in the length (l) of the block, which results in lower heat transfer, as discussed above.

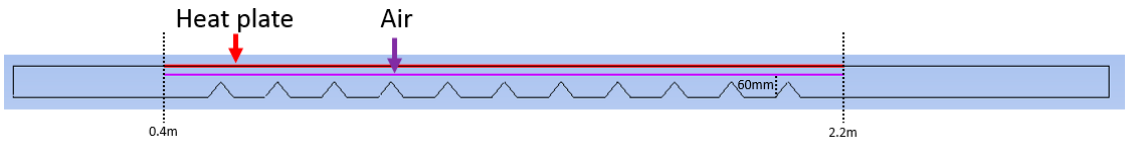

(**a**) Location for the temperature data of the heat plate and air

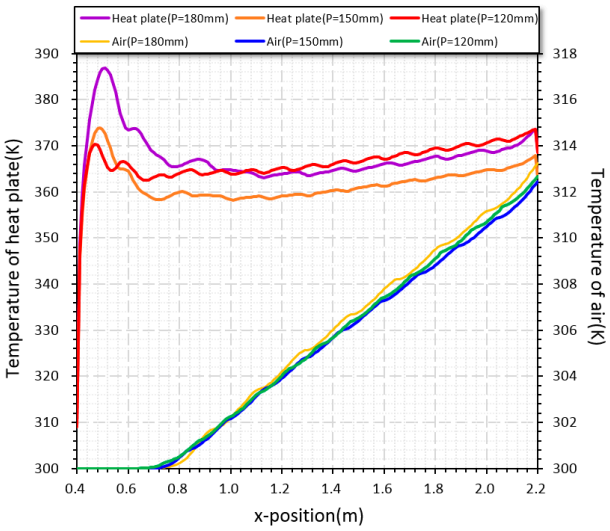

(**b**) Variation of temperature

Figure 7. Variation of temperature in the test section at Reynolds number of 12,000, for a fixed value of height (e = 40 mm) and length (l = 65 mm), and for different value of pitch (P).

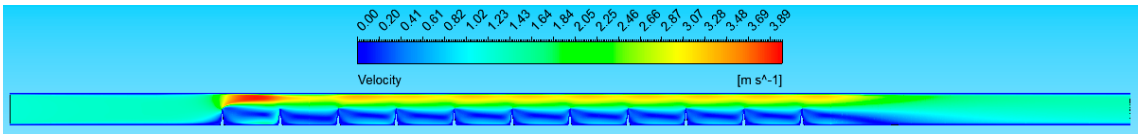

(**a**) l = 10 mm

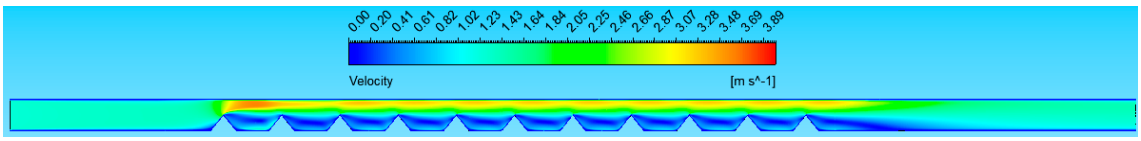

(**b**) l = 65 mm

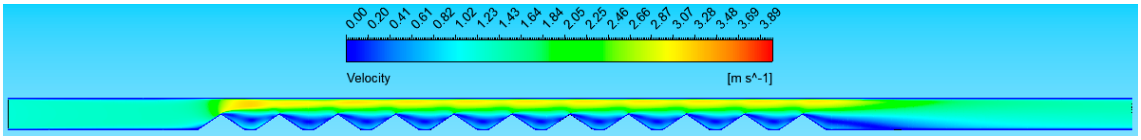

(**c**) l = 120 mm

Figure 8. Velocity contours at Reynolds number of 12,000 for a fixed value of pitch (P = 150 mm) and length (l = 65 mm), and different value of height (e).

Figure 9a–c shows the enhancement in Nusselt number. The enhancement in Nusselt number varied from 1.244 to 1.57, 1.806 to 2.183, and 2.919 to 3.374, respectively, for a height (*e*) of 20, 40, and 60 mm, for the range of Reynolds number investigated.

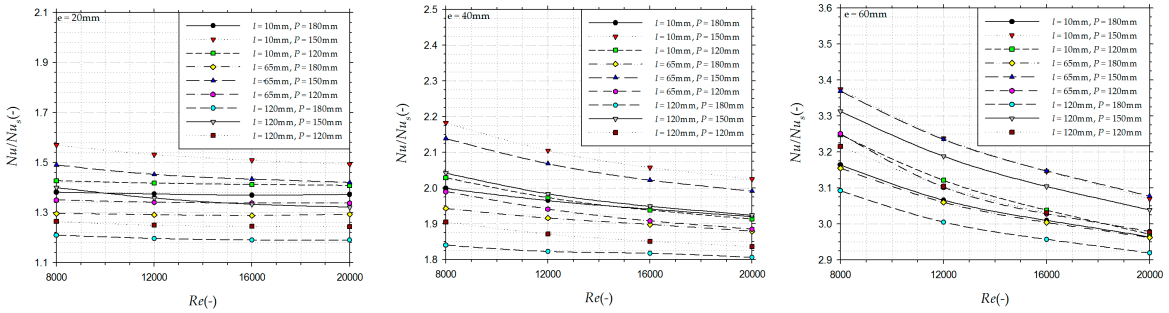

(**a**) e = 20 mm (**b**) e = 40 mm (**c**) e = 60 mm

Figure 9. Enhancement in Nusselt number for different value of pitch (*P*), length (*l*), and for a fixed value of height (*e*) with Reynolds number.

3.2. Flow Friction

In this section, the average flow-friction characteristics in a solar air duct with a transverse triangular block are presented as an average friction factor.

Figure 10a–c shows the variation of average friction factor for different values of pitch (*P*), length (*l*), and height (*e*) for transverse triangular block as a function of Reynolds number. In all cases, the installation of transverse triangular block leads to a higher average friction factor than that of a smooth air duct. The transverse triangular block, which was installed at the bottom of air duct, caused an obstruction of the flow. From the results, it is seen that the average friction factor decreases as the Reynolds number increases. This is due to the fact that the increasing value of the Reynolds number contributes to the greater suppression of the laminar sublayer.

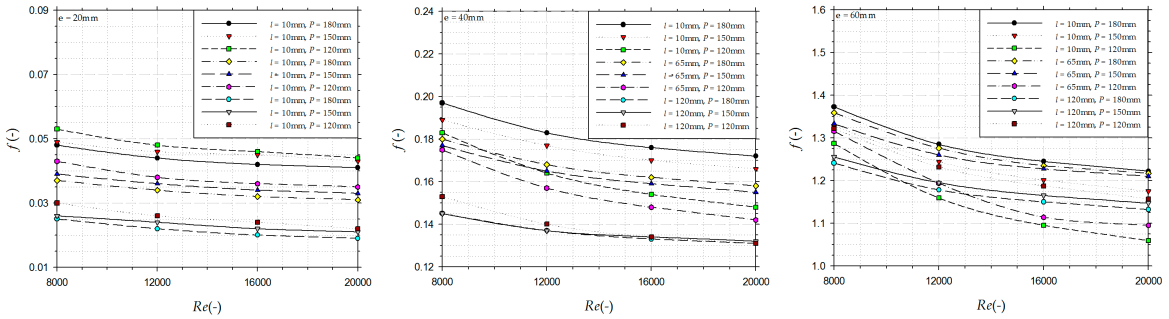

(**a**) e = 20 mm (**b**) e = 40 mm (**c**) e = 60 mm

Figure 10. Friction factor for different value of pitch (*P*), length (*l*), and for a fixed value of height (*e*) with Reynolds number.

It is also found that the average friction factor significantly increases as the block height (*e*) increases for a given value of Reynolds number, pitch (*P*), and length (*l*). This is due to the increase in interruptions in the flow path caused by the increasing value of the block height (*e*). Figure 11 shows the contours of pressure for different values of height (*e*) and for a fixed value of pitch (*P*), length (*l*), and Reynolds number. The contours remain similar, but the scale of pressure contours increases with the increase in height (*e*). This is because the increase in height (*e*) results in more interruptions in the flow path, as discussed above.

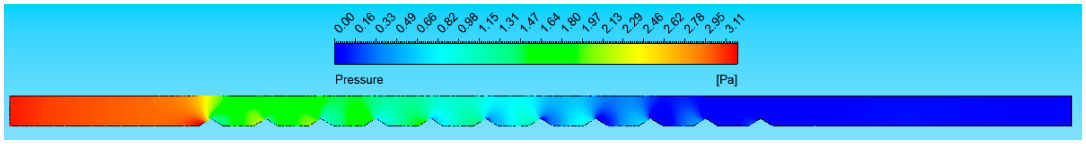

(**a**) e = 20 mm

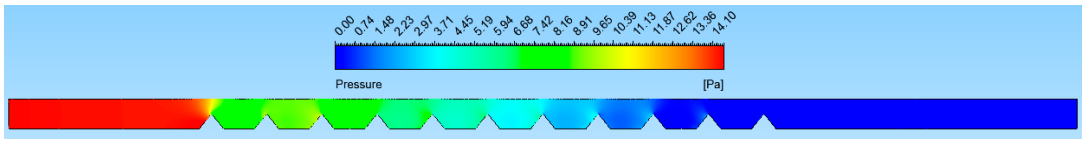

(**b**) e = 40 mm

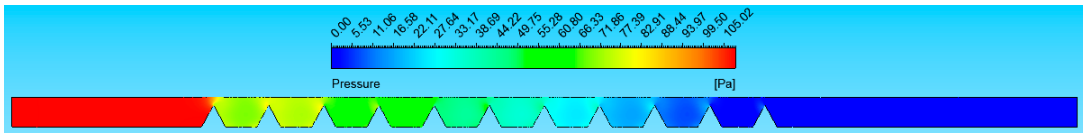

(**c**) e = 60 mm

Figure 11. Contours of pressure at Reynolds number of 12,000 for a fixed value of pitch (P = 150 mm) and length (l = 65 mm), and different value of height (e).

Moreover, it is seen that the average friction factor increases as the block pitch (P) decreases for a height (e) of 20 mm. This is because the number of blocks increases, resulting in more obstruction of the flow, as the pitch (P) decreases. However, the average friction factor tends to increase as the pitch (P) increases for the heights (e) of 40 and 60 mm. This may be due to the increase in the vortex region with decrease in pitch (P). The increase in the vortex region leads to higher eddy viscosity, which results in higher energy loss. Figure 12a–c shows the contours of eddy viscosity for different values of pitch (P) and for a fixed value of height (e), length (l), and Reynolds number. The scale of contours remains the same, but the structure of contours changes with the change in pitch (P). It can be seen that the eddy viscosity decreases with the decrease in pitch (P). The average friction factor tends to decrease as the block length (l) increases for a given value of height (e), pitch (P), and Reynolds number. This may be due to the decrease in the vortex region with the increase in the length (l).

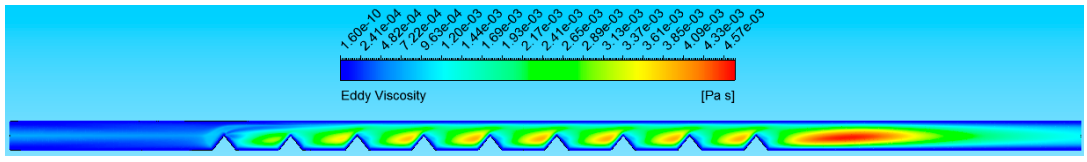

(**a**) P = 180 mm

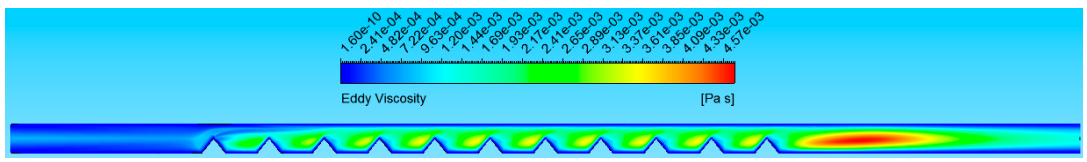

(**b**) P = 150 mm

Figure 12. *Cont.*

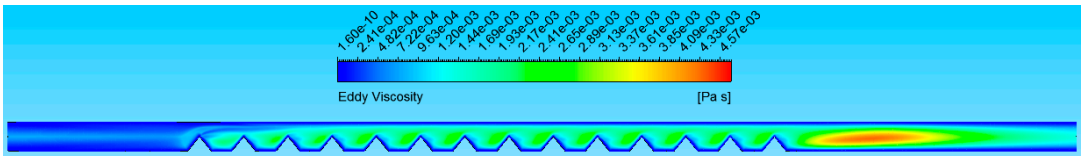

(**c**) P = 120 mm

Figure 12. Contours of eddy viscosity at Reynolds number of 12,000, for a fixed value of height (e = 40 mm) and length (l = 65 mm), and different value of pitch (P).

Figure 13a–c shows the enhancement in friction factor. The enhancement in friction factor was in the range of 2.675 to 6.211, 15.479 to 24.086, and 129.878 to 170.937, respectively, for a height (e) of 20, 40, and 60 mm, for the range of Reynolds number investigated.

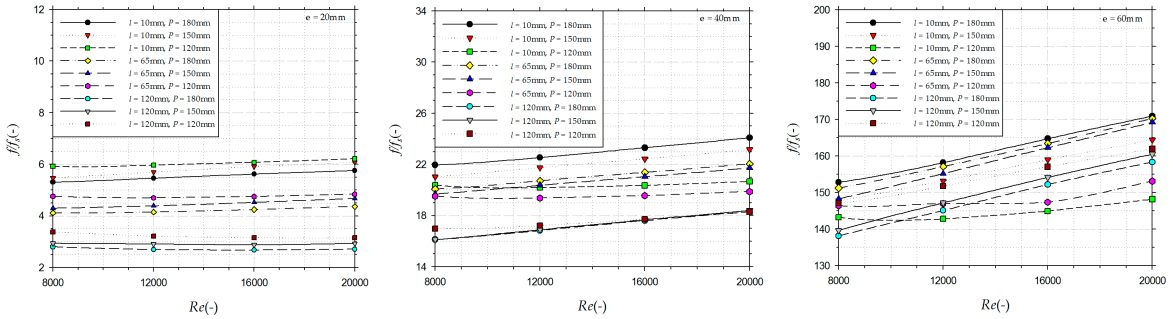

(**a**) e = 20mm (**b**) e = 40mm (**c**) e = 60mm

Figure 13. Enhancement in friction factor for different value of pitch (P), length (l), and for a fixed value of height (e) with Reynolds number.

3.3. Thermohydraulic Performance Parameter (THPP)

In this section, the thermohydraulic performance parameter (THPP), which evaluates the overall performance of a solar air heater, including both heat-transfer enhancement and increase in the friction factor, is presented.

Figure 14a–c shows the variation of THPP for different values of pitch (P), length (l), and height (e) for transverse triangular block as a function of Reynolds number. The values of THPP varied from 0.761 to 1.001, 0.661 to 0.827, and 0.531 to 0.654, respectively, for a height (e) of 20, 40, and 60 mm. In all cases, the THPP values increased with the decrease in Reynolds number. From the results, it is observed that the values of THPP increased as the height (e) decreased. Moreover, these values increased with the increase in length (l). However, in all cases, the maximum THPP was found for a pitch (P) value of 150 mm. Further increase or decrease in pitch (P) results in a decrease in THPP values. Therefore, it is concluded that the transverse triangular block installed at the bottom of the air duct is more effective for low Reynolds number, low height (e), and large length (l) for the pitch (P) of 150 mm. The highest value of THPP was found to be 1.001 for a height (e) of 20 mm, length (l) of 120 mm, and pitch (P) of 150 mm, at a Reynolds number of 8000, in the range of parameters investigated.

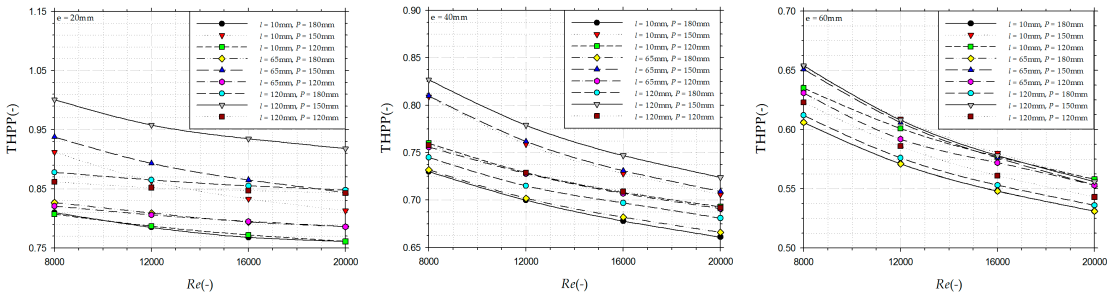

(**a**) e = 20 mm (**b**) e = 40 mm (**c**) e = 60 mm

Figure 14. Variation of THPP for different value of pitch (P), length (l), and for a fixed value of height (e) with Reynolds number.

4. Correlations for Nusselt Number (Nu) and Friction Factor (f)

To predict heat-transfer performance and fluid friction in the solar air heater having transverse triangular block at the bottom of air duct, the Nusselt number and friction factor need to be expressed as a function of the relative height (e/h), relative length (l/e), and relative pitch (P/e) for transverse triangular block and Reynolds number, considering similarity, as shown below:

$$Nu = \text{function of } (Re, e/\text{h}, P/e, l/e) \tag{14}$$

$$f = \text{function of } (Re, e/\text{h}, P/e, l/e) \tag{15}$$

In order to develop the correlation for Nusselt number, we first need to know the relationship between Nusselt number and Reynold number, and it is proportional to the nth power of Reynolds number as shown in Equation (16).

$$Nu = A_0 Re^n \tag{16}$$

The logarithmic form is as follows:

$$\ln(Nu) = \ln(A_0) + nln(Re) \tag{17}$$

At this time, a log–log plot can be used to obtain the values of coefficients A_0 and n. Figure 15 shows a graph of the $\ln(Nu)$ and the $ln\ (Re)$.

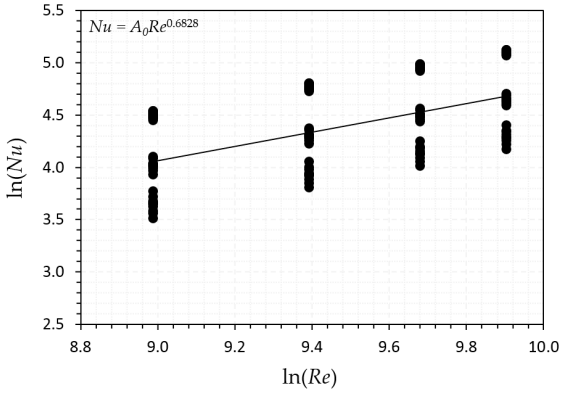

Figure 15. Plot of ln (Nu) as a function of ln (Re).

At this time, n, which is represented by a slope, is 0.6828. Therefore, Equation (16) can be written as Equation (18).

$$Nu = A_0 Re^{0.6828} \tag{18}$$

The coefficient A_0 is a function of the block height (e), length (l), and pitch (P). To develop the relationship between A_0 and relative height (e/h), a composite plot of $\ln\left(A_0 = Nu/Re^{0.6828}\right)$ versus $\ln(e/\mathrm{h})$ is shown in Figure 16.

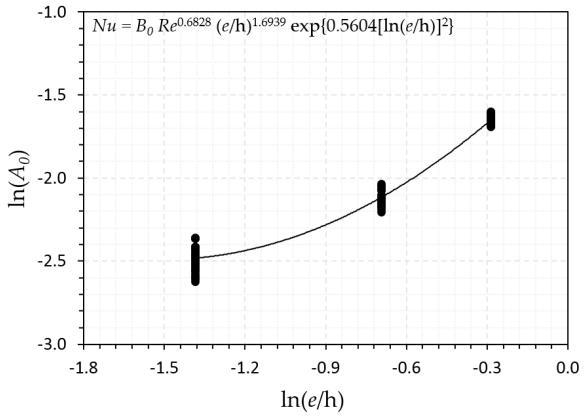

Figure 16. Plot of ln (A_o) as function of ln (e/h).

From the results, the relationship expressed as a polynomial of second-order was found to be best, and it results in Equation (19).

$$\ln(A_0) = \ln(B_0) + 1.6939\ln(e/\mathrm{h}) + 0.5604\{\ln(e/\mathrm{h})\}^2 \tag{19}$$

Equation (10) can be rearranged as follows:

$$A_0 = B_0(e/\mathrm{h})^{1.6939}\exp\left[0.5604\{\ln(e/\mathrm{h})\}^2\right] \tag{20}$$

or

$$Nu = B_0Re^{0.6828}(e/\mathrm{h})^{1.6939}\exp\left[0.5604\{\ln(e/\mathrm{h})\}^2\right] \tag{21}$$

Here, the B_0 is a function of relative length (l/e) and relative pitch (P/e). A similar plot between $\ln\left(B_0 = Nu/\{Re^{0.6828}(e/\mathrm{h})^{1.6939}\exp\left[0.5604\{\ln(e/\mathrm{h})\}^2\right]\}\right)$ and $\ln(l/e)$ is shown in Figure 17, and the relationship, which is written in Equation (22), was obtained.

$$B_0 = C_0(l/e)^{-0.0221}\exp\left[-0.0159\{\ln(l/e)\}^2\right] \tag{22}$$

or

$$Nu = C_0Re^{0.6828}(e/\mathrm{h})^{1.6939}\exp\left[0.5604\{\ln(e/\mathrm{h})\}^2\right](l/e)^{-0.0221}\exp\left[-0.0159\{\ln(l/e)\}^2\right] \tag{23}$$

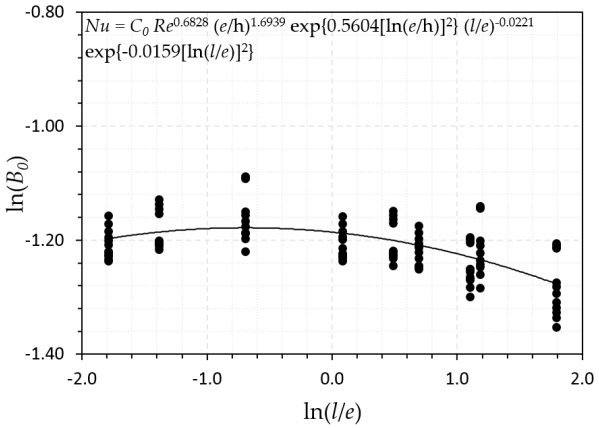

Figure 17. Plot of ln (B_0) as function of ln (l/e).

Here, the C_0 is a function of relative pitch (P/e). The relationship between the C_0 and relative pitch (P/e) can be obtained in a similar method. Figure 18 shows a composite plot of $\ln(C_0 = Nu/\{Re^{0.6828}(e/\mathrm{h})^{1.6939}\exp[0.5604\{\ln(e/\mathrm{h})\}^2](l/e)^{-0.0221}\exp[-0.0159\{\ln(l/e)\}^2]\}$ and $\ln(P/e)$, and the relationship was established as written in Equation (24).

$$C_0 = D_0(P/e)^{0.0563}\exp\left[-0.0122\left\{\ln(P/e\right\}^2\right] \tag{24}$$

or

$$Nu = D_0 Re^{0.6828}(e/\mathrm{h})^{1.6939}\exp[0.5604\{\ln(e/\mathrm{h})\}^2](l/e)^{-0.0221}\exp[-0.0159\{\ln(l/e)\}^2] (P/e)^{0.0563}\exp\left[-0.0122\{\ln(P/e)\}^2\right] \tag{25}$$

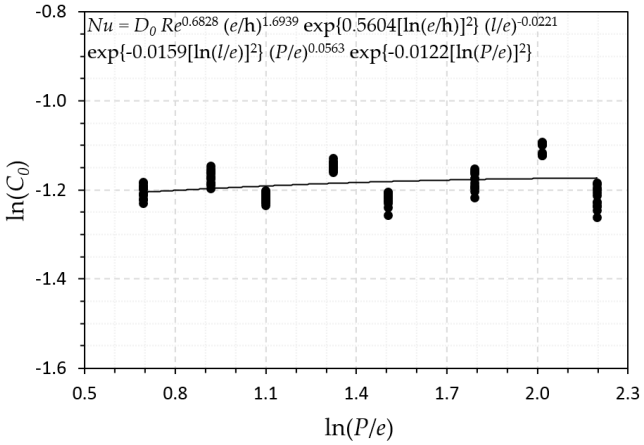

Figure 18. Plot of ln (C_0) as function of ln (P/e).

Here, the D_0 is constant, which can be obtained from the results in Figure 18. It was found that the constant has the value of 0.2899. Finally, the correlation for Nusselt number can be obtained through Equation (26).

$$Nu = 0.2899Re^{0.6828}(e/\mathrm{h})^{1.6939}(l/e)^{-0.0221}(P/e)^{0.0563}\exp[0.5604\{\ln(e/\mathrm{h})\}^2] \exp[-0.0159\{\ln(l/e)\}^2]\exp[-0.0122\{\ln(P/e\}^2] \tag{26}$$

Figure 19 shows a comparison of the Nusselt number values obtained by CFD simulation and predicted by developed correlation (Equation (26)). From the figure, it can be seen that most of the data fall within the deviation limit of ±12.5%, with the average absolute percentage deviation of 3.29%.

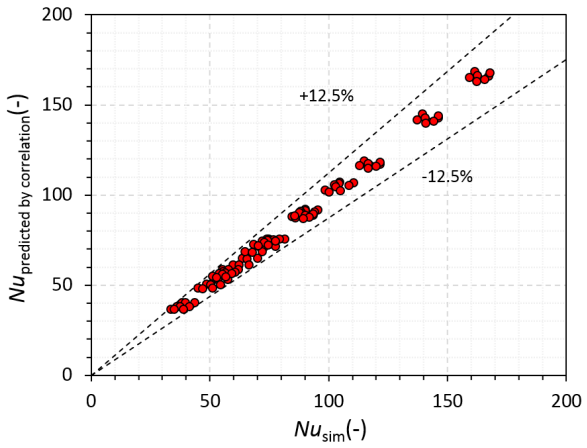

Figure 19. Comparison of simulation and predicted values of Nusselt number.

With the similar process, the correlation for friction factor has been developed as written in Equation (27).

$$f = 41.4049Re^{-0.1734}(e/\mathrm{h})^{7.5824}(l/e)^{-0.1015}(P/e)^{0.3427}\exp\left[2.5768\{\ln(e/\mathrm{h})\}^2\right] \exp\left[-0.0883\{\ln(l/e)\}^2\right]\exp\left[-0.1177\{\ln(P/e)\}^2\right] \quad (27)$$

Friction factor values obtained by CFD simulation and predicted by the developed correlation (Equation (27)) are compared in Figure 20. Most of the data fall within the deviation limit of 12.5%, with the average absolute percentage deviation of 7.92%.

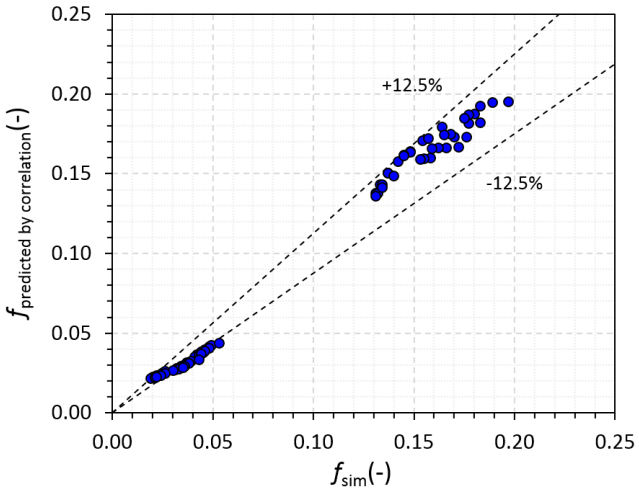

Figure 20. Comparison of simulation and predicted values of friction factor.

5. Conclusions

In the present work, a two-dimensional CFD analysis was carried out to study the effect of transverse triangular block installed at the bottom of air duct in a solar air heater on the Nusselt number and friction factor. The major conclusions of this study can be summarized as follows: (1) The parameters of the transverse triangular block have a strong effect on the Nusselt number and friction factor. The highest enhancement in Nusselt number was found at a low Reynolds number. However, contrary to this, the maximum enhancement in friction factor was seen in the high Reynolds number. (2) The enhancement in the Nusselt number was varied in the range of 1.244 to 1.57, 1.806 to 2.183, and 2.919 to 3.374 for a height (e) of 20, 40, and 60 mm, respectively. The maximum enhancement in Nusselt number was found to be 3.374 times higher than that of smooth duct and corresponds to a height (e) of 60 mm, pitch (P) of 150 mm, and length (l) of 10 mm, at a Reynolds number of 8000. (3) The enhancement in friction factor varied from 2.675 to 6.211, 15.479 to 24.086, and 129.878 to 170.937 for a height (e) of 20, 40, and 60 mm, respectively. A significant increase in the friction factor was found as the height (e) increased. The maximum enhancement in friction factor was found to be 170.937 times higher than that of smooth duct and corresponds to a height (e) of 60 mm, pitch (P) of 180 mm, and length (l) of 10 mm, at a Reynolds number of 20,000. (4) The THPP values increased with the increase in height (e), and with the decrease in length (l) and Reynolds number. However, in all cases, the highest value of THPP was found for a pitch (P) of 150 mm, and a further increase or decrease leads to the decrease in THPP value. The maximum value of THPP was found to be 1.001 for a height (e) of 20 mm, length (l) of 120 mm, and pitch (P) of 150 mm, at a Reynolds number of 8000. (5) The Nusselt number and friction-factor correlations were developed as a function of relative height (e/h), pitch (P/e), and length (l/e) for the block and Reynolds number, which can predict heat-transfer performance and flow friction in the solar air heater with a transverse triangular block at the bottom of the air duct, with the absolute percentage deviation of 3.29% and 7.92%, respectively. (6) This study, however, only focused on the heat-transfer enhancement and increase in friction factor by the transverse triangular

block in an air duct of the solar air heater. Thus, the other parameters, such as temperature increase and thermal efficiency of the collector, which have a transverse triangular block, need to be found in further studies, based on the results of this study.

Author Contributions: The authors made equal contributions and efforts in writing the manuscript. All authors have read and agreed to the published version of the manuscript.

Funding: This research received no external funding.

Acknowledgments: This study (Grants No. C0565944) was supported by the Business for Cooperative R&D between Industry, Academy, and Research Institute, funded Korea Small and Medium Business Administration in 2017, and was part of Hwi-Ung Choi's Doctor's thesis on a study on the performance improvement of air-based PV/T collector and the use of retrieved thermal energy.

Conflicts of Interest: The authors declare no conflicts of interest.

Nomenclature

Nu	Nusselt number (-)
Re	Reynolds number (-)
Pr	Prandtl number (-)
h	Convection heat transfer coefficients (W/m^2 K)
k	Thermal conductivity (W/m K)
D_h	Hydraulic diameter (m)
f	Friction factor (-)
ΔP	Pressure drop (Pa)
L	Length (m)
v	Air velocity (m/s)
e	Height of transverse triangular block (m)
P	Pitch of transverse triangular block (m)
l	Length of transverse triangular block (m)
e/h	Relative height of transverse triangular block (-)
P/e	Relative height of transverse triangular block (-)
l/e	Relative length of transverse triangular block (-)

Subscript

s	Smooth
b	Block

Greek Letters

ρ	Air density (kg/m^3)

References

1. Verma, S.K.; Prasad, B.N. Investigation for the optimal thermohydraulic performance of artificially roughened solar air heaters. *Renew. Energy* **2000**, *20*, 19–36. [CrossRef]
2. Alam, T.; Saini, R.P.; Saini, J.S. Effect of circularity of perforation holes in V-shaped blockages on heat transfer and friction characteristics of rectangular solar air heater duct. *Energy Convers. Manag.* **2014**, *86*, 952–963. [CrossRef]
3. Yadav, A.S.; Bhagoria, J.L. A CFD (computational fluid dynamics) based heat transfer and fluid flow analysis of a solar air heater provided with circular transverse wire rib roughness on the absorber plate. *Energy* **2013**, *55*, 1127–1142. [CrossRef]
4. Yadav, A.S.; Bhagoria, J.L. A CFD based thermo-hydraulic performance analysis of an artificially roughened solar air heater having equilateral triangular sectioned rib roughness on the absorber plate. *Int. J. Heat Mass Transf.* **2014**, *70*, 1016–1039. [CrossRef]
5. Yadav, A.S.; Bhagoria, J.L. A numerical investigation of square sectioned transverse rib roughened solar air heater. *Int. J. Therm. Sci.* **2014**, *79*, 111–131. [CrossRef]

6. Singh, S.; Singh, B.; Hans, V.S.; Gill, R.S. CFD (computational fluid dynamics) investigation on Nusselt number and friction factor of solar air heater duct roughened with non-uniform cross-section transverse rib. *Energy* **2015**, *84*, 509–517. [CrossRef]
7. Akpinar, E.K.; Koçyiğit, F. Experimental investigation of thermal performance of solar air heater having different obstacles on absorber plates. *Int. Commun. Heat Mass Transf.* **2010**, *37*, 416–421. [CrossRef]
8. Singh, A.P. Heat transfer and friction factor correlations for multiple arc shape roughness elements on the absorber plate used in solar air heaters. *Exp. Therm. Fluid Sci.* **2014**, *54*, 117–126. [CrossRef]
9. Singh, S.; Chander, S.; Saini, J.S. Heat transfer and friction factor correlations of solar air heater ducts artificially roughened with discrete V-down ribs. *Energy* **2011**, *36*, 5053–5064. [CrossRef]
10. Kumar, A.; Kim, M.-H. CFD Analysis on the Thermal Hydraulic Performance of an SAH Duct with Multi V-Shape Roughened Ribs. *Energies* **2016**, *9*, 415. [CrossRef]
11. Karim, M.A.; Hawlader, M.N.A. Development of solar air collectors for drying applications. *Energy Convers. Manag.* **2004**, *45*, 329–344. [CrossRef]
12. Ho, C.D.; Hsiao, C.F.; Chang, H.; Tien, Y.E.; Hong, Z.S. Efficiency of recycling double-pass V-corrugated solar air collectors. *Energies* **2017**, *10*, 875. [CrossRef]
13. Zheng, W.; Zhang, H.; You, S.; Fu, Y. Experimental investigation of the transpired solar air collectors and metal corrugated packing solar air collectors. *Energies* **2017**, *10*, 302. [CrossRef]
14. Kabeel, A.E.; Hamed, M.H.; Omara, Z.M.; Kandeal, A.W. Solar air heaters: Design configurations, improvement methods and applications–A detailed review. *Renew. Sustain. Energy Rev.* **2016**, *70*, 1189–1206. [CrossRef]
15. Gawande, V.B.; Dhoble, A.S.; Zodpe, D.B.; Chamoli, S. A review of CFD methodology used in literature for predicting thermo-hydraulic performance of a roughened solar air heater. *Renew. Sustain. Energy Rev.* **2016**, *54*, 550–605. [CrossRef]
16. Kumar, B.V.; Manikandan, G.; Kanna, P.R.; Taler, D.; Taler, J.; Nowak-Ocłoń, M.; Mzyk, K.; Toh, H.T. A performance evaluation of a solar air heater using different shaped ribs mounted on the absorber plate—A review. *Energies* **2018**, *11*, 3104. [CrossRef]
17. Alam, T.; Saini, R.P.; Saini, J.S. Heat and flow characteristics of air heater ducts provided with turbulators—A review. *Renew. Sustain. Energy Rev.* **2014**, *31*, 289–304. [CrossRef]
18. Ho, C.D.; Chang, H.; Hsiao, C.F.; Huang, C.C. Device performance improvement of recycling double-pass cross-corrugated solar air collectors. *Energies* **2018**, *11*, 338. [CrossRef]
19. Singh, S. Thermal performance analysis of semicircular and triangular cross-sectioned duct solar air heaters under external recycle. *J. Energy Storage* **2018**, *20*, 316–336. [CrossRef]
20. Norm, M. *Methods of Testing to Determine Thermal Performance of Solar Collectors: ASHRAE Standard 93*; ASHRAE: Washington, DC, USA, 2003.
21. Prasad, K.; Mullick, S.C. Heat transfer characteristics of a solar air heater used for drying purposes. *Appl. Energy* **1983**, *13*, 83–93. [CrossRef]
22. Prasad, B.N.; Saini, J.S. Effect of artificial roughness on heat transfer and friction factor in a solar air heater. *Sol. Energy* **1988**, *41*, 555–560. [CrossRef]
23. Karwa, R.; Solanki, S.C.; Saini, J.S. Heat transfer coefficient and friction factor correlations for the transitional flow regime in rib-roughened rectangular ducts. *Int. J. Heat Mass Transf.* **1999**, *42*, 1597–1615. [CrossRef]
24. Patankar, S.V. *Numerical Heat Transfer and Fluid Flow*; CRC Press: Boca Raton, FL, USA, 1980. [CrossRef]
25. Kumar, S.; Saini, R.P. CFD based performance analysis of a solar air heater duct provided with artificial roughness. *Renew. Energy* **2009**, *34*, 1285–1291. [CrossRef]
26. Pashchenko, D.I. ANSYS Fluent CFD Modeling of Solar Air-Heater Thermoaerodynamics. *Appl. Sol. Energy* **2018**, *54*, 32–39. [CrossRef]
27. Pashchenko, D.I. CFD Modeling of Operating Processes of a Solar Air Heater in ANSYS Fluent. *J. Eng. Phys. Thermophys.* **2019**, *92*, 73–79. [CrossRef]
28. Gupta, A.D.; Varshney, L. Performance prediction for solar air heater having rectangular sectioned tapered rib roughness using CFD. *Therm. Sci. Eng. Prog.* **2017**, *4*, 122–132. [CrossRef]
29. Singh, I.; Singh, S. CFD analysis of solar air heater duct having square wave profiled transverse ribs as roughness elements. *Sol. Energy* **2018**, *162*, 442–453. [CrossRef]
30. Singh, I.; Vardhan, S.; Singh, S.; Singh, A. Experimental and CFD analysis of solar air heater duct roughened with multiple broken transverse ribs: A comparative study. *Sol. Energy* **2019**, *188*, 519–532. [CrossRef]

31. Ansys Inc. *ANSYS Fluent 12.0 User's Guide*; Fluent Inc.: Lebanon, NH, USA, 2009. [CrossRef]
32. Webb, R.L.; Eckert, E.R.G. Application of rough surfaces to heat exchanger design. *Int. J. Heat Mass Transf.* **1972**, *15*, 1647–1658. [CrossRef]
33. Promvonge, P.; Thianpong, C. Thermal performance assessment of turbulent channel flows over different shaped ribs. *Int. Commun. Heat Mass Transf.* **2008**, *35*, 1327–1334. [CrossRef]
34. Eiamsa-ard, S.; Promvonge, P. Numerical study on heat transfer of turbulent channel flow over periodic grooves. *Int. Commun. Heat Mass Transf.* **2008**, *35*, 844–852. [CrossRef]